

Lambda-Field: A Continuous Counterpart Of The Bayesian Occupancy Grid For Risk Assessment And Safe Navigation

Journal Title
XX(X):1-16
©The Author(s) 2020
Reprints and permission:
sagepub.co.uk/journalsPermissions.nav
DOI: 10.1177/ToBeAssigned
www.sagepub.com/

SAGE

Johann Laconte¹, Abderrahim Kasmi^{1,4}, François Pomerleau², Roland Chapuis¹, Laurent Malaterre¹, Christophe Debain³ and Romuald Aufrère¹

Abstract

In the context of autonomous robots, one of the most important tasks is to prevent potential damages on the robot during navigation. For this purpose, it is often assumed to deal with known probabilistic obstacles, then to compute the probability of collision to each obstacle. However, in complex scenarios or unstructured environments, it might be difficult to detect such obstacles. In this case, a metric map is used where each position stores the information of occupancy. The most common type of metric map is the bayesian occupancy map. However, this type of map is not well fitted to compute risk assessment for continuous paths due to its discrete nature. Hence, we introduce a novel type of map called Lambda-Field, specially designed for risk assessment. We first propose a way to compute such a map and the expectancy of a generic risk over a path. Then, we demonstrate the utility of our generic formulation with a use case defining the risk as the expected force of collision over a path. Using this risk definition and the Lambda-Field, we show that our framework is capable of doing classical path planning while having a physical-based metric. Furthermore, the Lambda-Field gives a natural way to deal with unstructured environments like tall grass. Where standard environment representations would generate trajectories going around such obstacles, our framework allows the robot to go through the grass while being aware of the risk taken.

Keywords

Risk Assessment, Path Planning, Risk Modelling, Occupancy Grid, Safe Navigation, Field Robotics

1 INTRODUCTION

Autonomous robots are nowadays more and more visible in our life. They start to prove themselves useful in a very broad spectrum of applications, from autonomous driving to supporting humans in dangerous jobs like mining or search & rescue missions. One common aspect of every robot's tasks is the notion of safety: before taking any action, the robots have to assess the associated risk of the action.

To assess such a risk, robots need a way to represent and store the surrounding environment. In structured and controlled environments like warehouses, the easiest solution is to provide the robot a map of the environment as well as the position of every obstacle, robot and operator. Storing such objects leads to the construction of semantic maps, where each obstacle is stored as an object (e.g., wall, operator or robot). Under this representation, the robot has to keep track of every moving obstacle while not colliding the environment. However, such representation of the environment is not always available nor easy to build from raw data in all situations. For example, it is impossible to perfectly describe the underlying environment of a snowy forest or a crowded park. There is indeed a lot of unstructured obstacles in the first case that are not easily storable in such semantic maps, while in the second one a lot of dynamic obstacles hinder the construction of a precise map. Clustering raw data from Light Detection And Ranging

(lidar) measurements, as done by [Fulgenzi et al. \(2007\)](#) for example, might not be possible for the above scenarios.

When such high level environment representation is not available or possible, a lower level map is constructed, called metric map. Instead of storing features, the metric map tessellates the environment into cells, where each one stores the information of occupancy. This kind of map have been heavily studied and used since the beginning of robotics. These maps have been introduced by [Elfes \(1989\)](#) who proposed the concept of occupancy grids. Each cell stores the probability that the underlying environment is occupied, hence not traversable for the robot. This type of map is easy to construct and can be used to do a great variety of tasks like Simultaneous Localization And Mapping (SLAM) or path planning. However, as previously demonstrated by

¹ Université Clermont Auvergne, CNRS, SIGMA Clermont, Institut Pascal, F-63000 CLERMONT-FERRAND, FRANCE

² Northern Robotics Laboratory, Université Laval, Canada

³ Université Clermont Auvergne, INRAE, UR TSCF, 63178, Aubières, France

⁴ Sherpa Engineering, R&D Department, 333 Avenue Georges Clemenceau, 92000 Nanterre, France

Corresponding author:

Johann Laconte, Université Clermont Auvergne, CNRS, SIGMA Clermont, Institut Pascal, F-63000 CLERMONT-FERRAND, FRANCE

Email: johann.laconte@uca.fr

Heiden et al. (2017), a problem quickly arises when the robot wants to assess the probability of collision for a given path. Indeed, we are tempted to assess the probability of collision as the joint probability that every cell is free of obstacle. As an example, Figure 1 shows a robot crossing an environment where the probability of occupancy is 0.1 for each cell. Depending on the tessellation size, the probability of collision can be 0.19, or 0.34 for a tessellation half as small as the first one. This behavior comes from the fact that the correlation between the occupancy of two positions of the environment is not null. Nevertheless, it is impossible to accurately estimate this correlation. The same problem arises when dealing with occupancy grids stored in quad-trees (Kraetzschmar et al. 2004). Indeed, the robot could decide to cross a large high-probability cell instead of ten small low-probability ones.

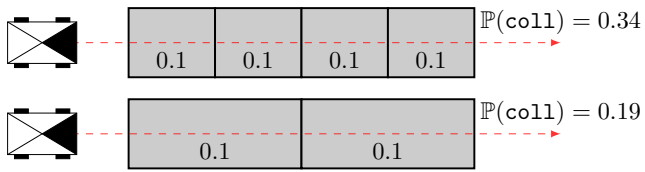


Figure 1. Example of collision assessment in occupancy grid. The robots (black boxes with their front represented as a filled triangle) want to cross an environment by following the dashed red line. The collision probability is uniform for the whole environment (0.1). The discretization size greatly influences the probability of collision, with the bottom scenario yielding to a safer path even though the underlying environment is the same.

Furthermore, the probability of collision is too simple to describe the risk in complex situations. For example, crossing a part of the environment at 5 km/h is not as risky as crossing the same environment at 70 km/h. Indeed, the damages caused by a potential collision are far more consequent at higher speed.

Under these considerations, we introduce the concept of Lambda-Field. The Lambda-Fields are a representation of the environment which allows the computation of the probability of collision while being independent of the tessellation size. They also give a natural way to assess more complex risks than the probability of collision. Our key contributions are

- A novel type of map called Lambda-Field, specially conceived to allow risk assessment;
- A mathematical formulation of risk assessment over a path; and
- A physical-based definition of the risk, defined as the expected force of collision in the case of ground vehicles.

In this paper, we provide a revised and extended version of our previous work (Laconte et al. (2019)). We give an extended theory that takes into account the mass of the obstacles, allowing the robot to evolve in unstructured environments. Moreover, we improve the theory of Heiden et al. (2017) to take into account the robot size and prove that the Lambda-Field is a generalization of their theory. We also extend our results with tests in real world conditions, in both structured and unstructured environments, showing that

Lambda-Fields allow behaviors that are impossible using classical occupancy grids.

2 RELATED WORK

In order to perform path planning, the first step is to construct a representation of the environment. In the context of unstructured or complex environments, a semantic map is impossible to create and a lower-level representation has to be used, called metric map. This kind of map tessellate the environment into cells where each one store the information of occupancy. The idea of tessellating the sensed environment was originally proposed by Elfes (1989). Later, Coué et al. (2006) enhanced this idea by adding a bayesian layer, which better handles uncertainty and noisy readings, increasing the robustness of the map. Many variations of the bayesian occupancy filter have been developed over the years, mainly adding dynamic obstacles in the grid. Saval-Calvo et al. (2017) wrote a review of the different Bayesian Occupancy Filter frameworks, presenting a taxonomy of the methods. O’Callaghan and Ramos (2012) proposed a way to store the occupancy map without discretization, using gaussian process. This method keeps the dependence between cells in the grid, which was not the case in the original occupancy grid from Elfes (1989). In an attempt to reduce the complexity of the gaussian process, Kim and Kim (2013) used overlapping local gaussian process. Regardless of this amelioration, the time computational complexity is still an issue for this kind of methods, whereas the standard occupancy grids as well as our method do not suffer from such problem. Ramos and Ott (2016) developed an analog method using Hilbert maps, overcoming the computational complexity of the gaussian process. In order to take into account the uncertainty in the different parameters, the method has been extended to bayesian Hilbert maps by Senanayake and Ramos (2017). Lately, HM have been generalized to dynamic environment by Guizilini et al. (2019), allowing real-time occupancy predictions. These methods still need parameters to tune that have great consequences on the quality of the resulting map. An alternative algorithm for occupancy grid has been presented in Agha-mohammadi et al. (2019) by storing richer data in a map, taking into account the estimation of the variance for each cell. Under these considerations, our framework is very alike the bayesian occupancy grid, as the environment is tessellated into cells. The Lambda-Field also stores a confidence interval over each cell in the same fashion as Agha-mohammadi et al. (2019).

Once a representation of the environment is available, the robot can start to assess risk in its map. The risk was first defined by the likelihood not to collide anything as said by Fraichard (2007). In the context of autonomous driving, the Time-To-Collision introduced by Lee (1976) is widely used. This metric measures the time at which the robot will collide with a specific obstacle given the current path. The Time-To-Collision is useful in accident mitigation systems, but is not well fitted for long-term planning. It has been demonstrated by Laugier et al. (2011) that the Time-To-Collision lacks context hence is not the best solution for every situation. Furthermore, this kind of metric is used in the context of known dynamics obstacles and is not easily transposable for

path planning algorithms. Indeed, the Time-To-Collision is mainly useful to mitigate the speed of a vehicle in traffic. Given these factors, the risk has to be defined in another fashion in the context of path planning in occupancy grids.

The risk is also very dependant on the application. For example, [Vaillant et al. \(1997\)](#) or [Caborni et al. \(2012\)](#) tackle the problem of path planning for Neurosurgery. For this application, the risk depends essentially on which zones of the brain the tool goes through. It is very different from standard path planning risks as in this context we are sure to collide with a part of the brain for every possible path. In that sense, path planning framework should be able to tackle different type of risks, which is the case of the Lambda-Field.

[Majumdar and Pavone \(2020\)](#) address the issue of how should a robot quantify risk and what constitutes a ‘good’ risk metric. It comes to the conclusion that a risk measure is said to be coherent if it satisfies axioms, showing that otherwise, the risk metric can have undesired behaviors. However, the physical meaning is neglected which leads to non-intuitive definitions for risk metric and difficult parameter settings for path planning. In our work, we thereupon define the risk as an understandable quantity, which is for our application the expected force of collision on a given path. Our metric also respect the axioms defined by [Majumdar and Pavone \(2020\)](#), leading to a risk proven to behave as desired as well as having a physical unit.

In the context of occupancy grid, a risk map is widely used to deal with the risk. For path planning, the occupancy grid is replaced with a risk map, where each cell stores the risk at this position. The higher the risk, the more the robot should avoid this place while planning its trajectory. [Tsiotras and Bakolas \(2007\)](#) used wavelets to store the environment and a risk map at different scales: For this application, the risk was defined as the probability of occupancy. The path planning method was then to find the path minimizing the overall sum of the risk of each traversed cell. Hence, the total risk lacks physical meaning. Our framework differs from the above one as the total risk of a path has the same unit as the used risk metric. In another context, [De Filippis et al. \(2011\)](#) used a risk map to control the altitude of an unmanned aerial vehicle. The risk is defined as the probability to fly in unsafe conditions for a given point on the map. In the same fashion, [Primatesta et al. \(2019\)](#) defined the risk as the hourly probability of lethal incidents for each position of the unmanned aerial vehicle. The risk is also set to the maximum for obstacles and no-fly zones. [Joachim et al. \(2008\)](#) used a risk map to prevent the robot from going too close to dangerous obstacles like pedestrians or other cars, allowing the robot to safely navigate in narrow spaces like parking spots. [Pereira et al. \(2011\)](#) also used a risk map to find the best path for underwater vehicles, where the risk was set to the probability that the position is occupied by an obstacle. Although all these methods demonstrate good results, they all assume that the risk is only a function of the position, omitting the robot configuration. As said before, the robot configuration can greatly change the risk, as for example, going to a position at high speed is often more dangerous than going at low speed. [Feyzabadi and Carpin \(2014\)](#) defined a risk function that depends on the position as well as the robot action. As a result, the robot can choose to go to a position only if its speed is low enough. Our framework uses

the same idea while giving a physical meaning to the cost of the overall path. Thereupon, the probability of collision is a metric too simple to perfectly describe the risk. As said by [Eggert \(2014\)](#), in the case of ADAS systems, we better want to assess the expected damage done to the vehicle than the probability of collision. We then propose a framework allowing the computation of a generic risk that can be defined depending on the application.

Using its representation of the environment and a risk function, the robot can start planning. Many of the popular methods use a binary representation of the environment, meaning that any point in the environment is either free or occupied. A review of such algorithms can be found in [Tsardoulias et al. \(2016\)](#). The most common way to convert the bayesian grid into a binary grid is to apply a user-defined threshold as done by [Yang et al. \(2013\)](#). However, applying a threshold to the environment might lead to discard some obstacles, conducting the robot to plan into possible occupied zones. A review of algorithms of path planning in occupancy grids has been done by [Čikeš et al. \(2011\)](#). The different algorithms presented in this article all want to minimize the cost function of the path, which is the sum of the cost of each traversed cells. The cost of a path has no physical meaning, which implies that determining if the path is truly safe might become a difficult task.

Another method proposed by [Fulgenzi et al. \(2007\)](#) is to cluster the occupancy grid, leaving the unclustered space as free or occluded. The risk assessment is then reduced to assessing the risk for probabilistic known obstacles. However, such clustering can be very difficult to compute in unstructured environment. We thus need a way to evaluate the cost of a path in occupancy grids, taking into account the probability of occupancy. Using Rapidly-exploring Random Tree, [Fulgenzi et al. \(2008\)](#) and [Fulgenzi et al. \(2009\)](#) defined the cost of a path as the joint probability of not having a collision in each node. It assumes that traveling between nodes is risk-free: if we do not make this assumption, we fall back on the initial problem to compute a cost over a continuous path. To overcome the problem of computation of the risk over a continuous path, several methods have been proposed. [Rummelhard et al. \(2014\)](#) defined the risk in a Bayesian occupancy grid as the maximum probability of collision over the cells. Nevertheless, there is no natural way to include a more complicated risk in the framework and these metrics can show unintended behaviors in complicated scenarios. Indeed, traversing one high probability cell has the same risk as traversing ten cells of the same probability for the second metric. [Dhawale et al. \(2018\)](#) chose to represent the environment as a gaussian process and represented the obstacles using a threshold over the gaussians. Doing such method thereby dissociates free space and occupied space, falling back on the methods presented in [Tsardoulias et al. \(2016\)](#). [Gerkey and Konolige \(2008\)](#) computed the cost of a path by summing the probability of occupancy of the cells the path crosses. This sum is then injected into a global cost function, taking into account other constraints like the speed or the distance to the objective, where each constraint has a user-defined coefficient. [Francis et al. \(2018\)](#) used the same idea for path planning in Hilbert Maps, introduced by [Ramos and Ott \(2016\)](#). The drawback of these methods is that the cost lacks physical meaning as we sum probabilities.

Since this sum does not have any physical unit, its associated coefficient does not have one either, making its tuning non-intuitive for the user. Finally, [Heiden et al. \(2017\)](#) used the concept of product integral to compute the probability of collision over a path. It leads to a probability of collision, but this method has no physical meaning. We show in this article that our framework can be seen as the generalization of their framework.

3 THEORETICAL FRAMEWORK

We present in this section the theoretical framework to assess a generic risk over a path in Lambda-Fields. First, we justify the use of the mathematical tools by showing how they naturally arise while dealing with continuous environments. Then, we address the construction of the Lambda-Fields in [subsection 3.1](#), as well as way to compute confidence intervals over the field in [subsection 3.2](#). Indeed, the robot should not be as confident of moving if it measures the cell in front of it one or a hundred times empty. Next, we present in [subsection 3.3](#) a framework capable of assessing a generic risk over a path in a Lambda-Field. We then use this framework to create a risk function allowing the robot to navigate in unstructured environment like tall grass in [subsection 3.4](#). Finally, we improve the framework of [Heiden et al. \(2017\)](#) in [subsection 3.5](#) to take into account the size of the robot and show that it can be seen as a special case of our framework. It can be summarized using [Figure 2](#): for the robot to reach its goal, it first needs to map its surrounding environment, hence construct a Lambda-Field with confidence intervals over the values. Once the robot has such a map, it can assess the risk of a given path and choose the best one to reach its goal.

The key concept of the Lambda-Field is its ability to assess the probability of collision inside a subset of the environment, then leading to the computation of expectancy of risk. To better understand the reasons of the following framework, we will first demonstrate its construction. We assume that the probability of encountering a collision for a path of area Δa is $\lambda_i \Delta a$, where λ_i is the ‘rate’ of the event collision and $\Delta a \rightarrow 0$. The larger λ_i is, the more likely a collision will happen. The probability of crossing N surfaces of area Δa with a rate λ_i without collision is

$$\prod_{i=0}^{N-1} (1 - \lambda_i \Delta a). \quad (1)$$

Taking the limit of the path area $\Delta a \rightarrow 0$ leads to the computation of the Volterra type I product integral. For a path crossing a total area of A where each subregion of area Δa has a rate $\lambda(a)$, a being the total area crossed from the beginning, we have

$$\lim_{\Delta a \rightarrow 0} \prod_{i=0}^{A/\Delta a} (1 - \lambda(i\Delta a)\Delta a) = \exp\left(-\int_0^A \lambda(a) da\right). \quad (2)$$

A proof of the above equation can be found in [Slavík \(2007\)](#). The probability of encountering no collision over a path is

then the probability that no event ‘collision’ happens in a heterogeneous Poisson point distribution of rate $\lambda(a)$. Taking the limit of a binomial distribution indeed leads to a Poisson point process distribution. Hence, the natural way of dealing with collisions in a continuous manner is to use Poisson point process distribution.

This process counts the number of events which have happened given a certain area, depending on the mathematical space. In our case, we want to count the number of the event ‘collision’ which could occur given a path (i.e., a subset of \mathbb{R}^2). We point out that the theory is here presented for 2D paths, but the extension in \mathbb{R}^3 is trivial, as the only change is the tessellation of the map being in 3D instead of 2D.

For a positive scalar field $\lambda(x)$, with $x \in \mathbb{R}^2$, the probability to encounter at least one collision in a path $\mathcal{P} \subset \mathbb{R}^2$ is

$$\mathbb{P}(\text{coll}|\mathcal{P}) = 1 - \exp\left(-\int_{\mathcal{P}} \lambda(x) dx\right). \quad (3)$$

Nonetheless, it is impossible to both compute and store the field $\lambda(x)$ as it has an infinite number of degrees of freedom. Hence, we discretize our field into cells in a similar fashion to Bayesian occupancy grids. Tessellating the field, the probability of collision is approximated by

$$\mathbb{P}(\text{coll}|\mathcal{P}) \approx 1 - \exp(-\Lambda(\mathcal{C}))$$

with $\Lambda(\mathcal{C}) = \Delta a \sum_{c_i \in \mathcal{C}} \lambda_i,$ (4)

for a path \mathcal{P} crossing the cells $\mathcal{C} = \{c_0, \dots, c_N\}$, where each cell c_i has an area of Δa and an associated lambda λ_i , which is the intensity of the cell. The lambda can be seen as a measure of the density of the cell: the higher the lambda is, the most likely a collision will happen in this cell.

Using this representation, we hereby see that the probability of collision is not dependent on the size of the cells. It is indeed the same to compute the probability of collision for crossing two cells of area $\Delta a/2$ or one cell of area Δa for a constant λ . As a concrete example, [Figure 2](#) gives a path a robot might follow, as well as the underlying cells (of area 0.04 m^2) it crosses. The robot crosses 58 cells with $\lambda_i = 0.1$ and one cell with $\lambda_i = 2$. Using [Equation 4](#), the probability of collision is evaluated at 0.27. One can note that this probability of collision is independent of the tessellation size while naturally arising from the theory.

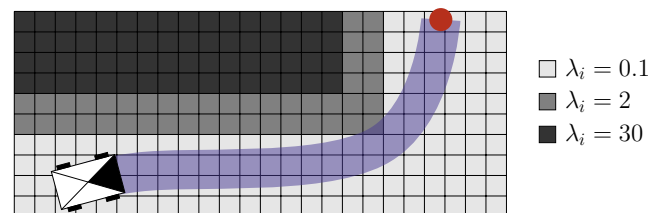


Figure 2. The robot wants to go to the position in red. In blue, the actual path the robot follows. Each cell has an area of $\Delta a = 0.04 \text{ m}^2$. Using [Equation 4](#), the probability of collision in this path is 0.27.

3.1 Computation of the field

As we established a new approach to represent the occupancy of an environment, we need to develop a way to dynamically compute the lambdas. We assume that the robot is equipped with a lidar sensor, which gives us a list of cells crossed by beams without collision, and another list of cells where the beams collided. Using this sensor model, we construct the Lambda-Field in the following manner. We want to find the combination of $\lambda = \{\lambda_i\}_{i \in \llbracket 0, C-1 \rrbracket}$, for a map tessellated into C cells, that maximizes the expectation of the K beams the lidar has shot since the beginning. Also, each lidar beam has an associated error region \mathcal{E}_k of area e_k centered on the measurement, meaning that the actual obstacle is in \mathcal{E}_k . **Figure 3** shows an example of such lidar beam error region.

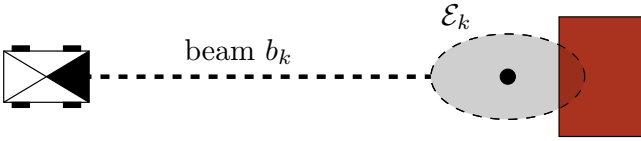


Figure 3. The robot measures an obstacle using a lidar sensor. The obstacle (in red) is in the area \mathcal{E}_k (in gray) centered on the measurement (black dot).

Therefore, each lidar collision gives a region where an obstacle is. This kind of sensor simplification is common and is used for example by [Rohou et al. \(2018\)](#). At this stage, we assumed that every lidar measurement possesses the same error region area e . The case where each lidar beam has a different error region is dealt in [Appendix A](#). For each lidar beam b_k , the beam crossed without collision the cells $c_m \in \mathcal{M}_k$ and hit an obstacle contained in the cells $c_h \in \mathcal{E}_k$. The log-likelihood of the beam b_k is

$$\mathcal{L}(b_k|\lambda) = \ln \left[\exp(-\Lambda(\mathcal{M}_k)) \left(1 - \exp(-\Lambda(\mathcal{E}_k))\right) \right]. \quad (5)$$

The log-likelihood of K lidar beams is then

$$\begin{aligned} \mathcal{L}(\{b_k\}_{0:K-1}|\lambda) &= \sum_{k=0}^{K-1} \mathcal{L}(b_k|\lambda) \\ &= \sum_{k=0}^{K-1} \left[-\Lambda(\mathcal{M}_k) + \ln \left(1 - \exp(-\Lambda(\mathcal{E}_k))\right) \right]. \end{aligned} \quad (6)$$

We want to maximize this quantity, hence nullify its derivative as the function is concave. In order to find a closed-form, we approximate the derivative with the assumption that the variation of lambda inside the error region of the lidar is small enough to be negligible. Thus, for each $\lambda_i \in \mathcal{E}_k$ we have

$$\Delta a \sum_{c_h \in \mathcal{E}_k} \lambda_h \approx e \lambda_i. \quad (7)$$

Using this approximation, the derivative is

$$\frac{\partial \mathcal{L}(\{b_k\}_{0:K-1}|\lambda)}{\partial \lambda_i} \approx -m_i \cdot \Delta a + h_i \frac{\Delta a}{\exp(e \lambda_i) - 1}, \quad (8)$$

where m_i is the number of times the cell c_i has been counted as ‘miss’ (i.e., was outside the error region) and h_i is the

number of times the cell c_i has been counted as ‘hit’ (i.e., was in the error region of the sensor). We finally find the zero of the derivative, leading to

$$\lambda_i = \frac{1}{e} \ln \left(1 + \frac{h_i}{m_i} \right). \quad (9)$$

This closed-form allows a low computation complexity of the lambda field. We also see that the formula is independent of the size of the cells, which is the main limitation of current representation we were aiming at resolving.

We are then able to construct the Lambda-Field using [Equation 9](#).

3.2 Confidence intervals

In the same way as [Agha-mohammadi et al. \(2019\)](#), we define the notion of confidence over the values in the Lambda-Field. Indeed, the robot should not be as confident to pass through a cell if it measured it once or a hundred times. For each cell c_i , we seek the bounds λ_L and λ_U such that

$$\begin{aligned} \mathbb{P}(\lambda_L \leq \lambda_i \leq \lambda_U) &\geq 95\% \\ \Leftrightarrow \mathbb{P}(\lambda_L \leq \frac{1}{e} \ln \left(1 + \frac{h_i}{m_i} \right) \leq \lambda_U) &\geq 95\%. \end{aligned} \quad (10)$$

To compute those bounds, we introduce the notion of false positives and false negatives: every cell measurement j has a probability p_j^h to be rightfully read ‘hit’ and a probability p_j^m to be rightfully read ‘miss’. The probabilities p_j^h and p_j^m have to be experimentally computed and can vary according to a great number of parameters: for example, the probability p_j^h is lower in the event of heavy rain or snow.

Using the relation $h_i = M - m_i$ where M is the number of times the cell has been measured, we can rewrite the above equation as

$$\mathbb{P}(K_L \leq h_i \leq K_U) \geq 95\%, \quad (11)$$

such that

$$\begin{aligned} \lambda_L &= \frac{1}{e} \ln \left(\frac{K_L}{M - K_L} + 1 \right), \\ \lambda_U &= \frac{1}{e} \ln \left(\frac{K_U}{M - K_U} + 1 \right). \end{aligned} \quad (12)$$

The quantity h_i can be seen as a sum of M Bernoulli distributions, such that

$$h_i = \sum_{j=0}^{h_i-1} \bar{h}_j + \sum_{j=0}^{m_i-1} (1 - \bar{m}_j), \quad (13)$$

where \bar{h}_j and \bar{m}_j are Bernoulli variables equal to 1 if the reading was right and 0 otherwise. The quantity $\sum_j (1 - \bar{m}_j)$ is hence the number of times the sensor wrongfully reads ‘hit’ instead of ‘miss’.

The distribution of h_i is not binomial, but a Poisson binomial distribution with poor behaviors in terms of computation. Since the Poisson binomial distribution satisfies the Lyapunov central limit theorem, we can approximate its distribution with a Gaussian distribution of

same mean and variance:

$$\begin{aligned} \mu &= \sum_{j=0}^{h_i-1} p_j^h + \sum_{j=0}^{m_i-1} 1 - p_j^m \quad \text{and} \\ \sigma^2 &= \sum_{j=0}^{h_i-1} p_j^h(1 - p_j^m) + \sum_{j=0}^{m_i-1} p_j^m(1 - p_j^m). \end{aligned} \quad (14)$$

We can then have the bounds at 95% for example, with

$$\begin{aligned} K_L &\approx \max(\mu - 1.96\sigma, 0), \\ K_U &\approx \min(\mu + 1.96\sigma, M). \end{aligned} \quad (15)$$

The bounds λ_L and λ_U are then retrieved from K_L and K_U using Equation 12.

As an example of this bound computation, Figure 4 shows the behavior of the confidence interval for different confidences, where the probability of wrong measurement is the same for every measurement. The lidar measures an empty cell c_i . The confidence interval quickly decreases as the number of readings ‘miss’ increases. At the 40th measurement, the lidar misreads and returns a ‘hit’. The confidence interval grows around the expected lambda computed with Equation 9 before re-converging.

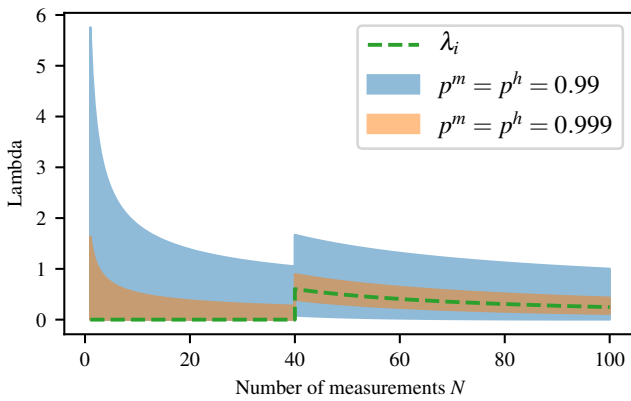


Figure 4. Convergence of the confidence intervals for a free cell c_i . At the fortieth measurement, the sensor misreads the cell and returns a ‘hit’. The confidence interval grows around the expected λ_i before re-converging.

3.3 Generic framework for risk assessment

As said before, the motivation of the Lambda-Fields is its ability to compute path integral, hence a risk along a path. This risk can be defined depending on the application and is independent of the following framework, meaning that it can be interchanged without any modification of the theory. For a path $\mathcal{P} \subset \mathbb{R}^2$ crossing in order the cells $\mathcal{C} = \{c_i\}_{0:N}$, the probability distribution function over the Lambda-Field is

$$f(a) = \exp\left(n\Delta a\lambda_n - \Delta a \sum_{i=0}^{n-1} \lambda_i\right) \cdot \lambda_n \exp(-a\lambda_n), \quad (16)$$

where $n = \lfloor a/\Delta a \rfloor$ and $\lfloor \cdot \rfloor$ is the standard floor function. The variable a denotes the area the robot has crossed. Figure 5 shows an example of the probability density for a given path on a Lambda-Field: when the robot goes through high-lambda cells, the cumulative distribution probability

quickly increases to one. One can note that it is quite easy to convert a into the curvilinear abscissa, which is far more convenient to link to the speed. For a robot of width W which has crossed an area a , its curvilinear abscissa s equals to

$$s = \frac{a}{W}. \quad (17)$$

Furthermore, Equation 16 can be easily proved as integrating $f(a)$ over a certain path \mathcal{P} crossing the cells $\mathcal{C} = \{c_i\}_{0:N-1}$ gives the probability of encountering at least one collision:

$$\mathbb{P}(\text{coll}|\mathcal{P}) = \int_0^{N\Delta a} f(a) da = 1 - \exp(-\Lambda(\mathcal{C})). \quad (18)$$

We can then define the expectation of a risk function $r(\cdot)$ over the path, defined as

$$\mathbb{E}[r(A)] = \int_0^{N\Delta a} f(a)r(a) da. \quad (19)$$

The random variable A denotes the crossed area at which the first event ‘collision’ occurs. If the cells are small, we can assume that the function $r(\cdot)$ is constant inside each cell. Using this assumption, we simplify the above equation to

$$\begin{aligned} \mathbb{E}[r(A)] &= \sum_{i=0}^{N-1} K_i r(\Delta ai), \quad \text{with} \\ K_i &= \exp(-\Lambda(\{c_j\}_{0:i-1})) \left[1 - \exp(-\Lambda(\{c_i\}))\right], \end{aligned} \quad (20)$$

for a path \mathcal{P} going through the cells $\{c_i\}_{0:N-1}$. Note that $\{c_i\}$ is a singleton whereas $\{c_j\}_{0:i-1}$ contains i elements.

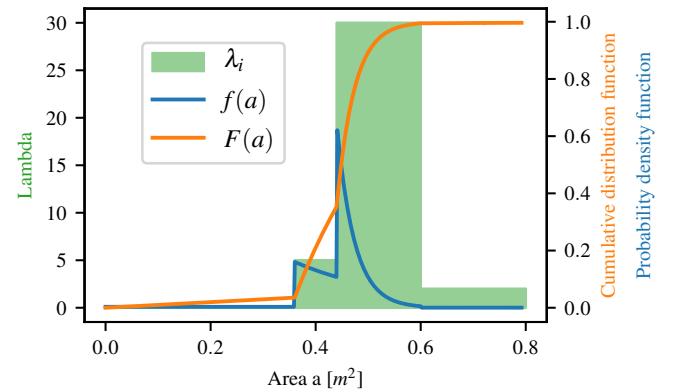


Figure 5. Example of lambda field the robot crosses (in green), with the associated probability density $f(a)$ (in blue) and cumulative distribution $F(a)$ (in orange).

The risk function $r(\cdot)$ is generic and can take into account the state of the robot as well as the state of the world. One can notice that the special case $r(\cdot) = 1$ leads to the probability of collision given by Equation 4. Furthermore, the probability density $f(a)$ only looks at the risk generated by the first collision occurring on the path. Therefore, it is assumed that the robot stops after any collision and does not continue its course. This assumption can be lifted if necessary, as shown in the next section.

For our applications, we chose to model the risk as the force of collision (i.e., loss of momentum) if the collision

occurred at the area a . It is indeed a good quantification of the damage induced by the collision and is a better metric of the risk than the probability of collision (Eggert 2014). First, we present as an example a way to assess this risk assuming that every obstacle has an infinite mass. Indeed, this assumption holds for most scenarios where the robot's mass is negligible compared to the obstacles masses (e.g., a tree or a wall). We then remove this assumption in subsection 3.4 where each obstacle now has a probabilistic mass, allowing the robot to evolve in unstructured environments.

Assuming the obstacle that the robot collides have an infinite mass, the force of collision is computed as

$$r(a) = m_R \cdot v_R^n(a), \quad (21)$$

where m_R is the mass of the robot, and $v_R^n(a)$ is its velocity towards the obstacle at the area a . As shown in Figure 6, the velocity towards the obstacle of normalized normal \mathbf{n} is

$$\begin{aligned} v_R^n &= \left| \mathbf{n}^T \mathbf{v}_R \right| \\ &= \left| v_R \cdot \cos(\theta) \right| \quad \text{for } \|\mathbf{n}\| = 1 \end{aligned} \quad (22)$$

where \cdot^T stands for the usual vector transpose, $v_R = \|\mathbf{v}_R\|$ the robot velocity and θ the angle between the robot heading and the obstacle's normal. The angle of collision is interesting to take into account for numerous scenarios, as for example an autonomous vehicle driving over a cliff. Because of skidding, the vehicle may find itself in a configuration where it has no choice but to collide the safety railing. The best choice will naturally be to minimize the collision, hence collide the railing with a high incidence angle.

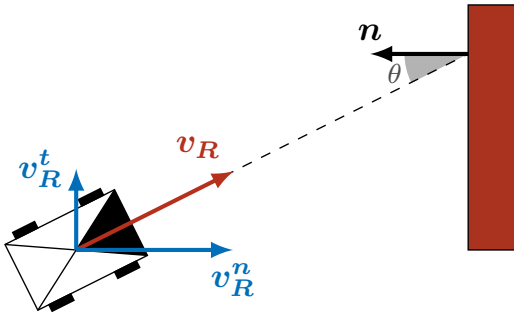


Figure 6. The robot of speed $v_R = \|\mathbf{v}_R\|$ collides with an obstacle of normal \mathbf{n} with an angle θ . The speed of the robot can be decomposed into the tangential component v_R^t and the normal component v_R^n . Only the latter influences the collision with the obstacle.

This risk metric assumes that every obstacle the robot might encounter has an infinite mass. We also assume perfect inelastic collision, as most deployed vehicles are designed to absorb collisions as much as possible. It means that if the robot collides with an obstacle, the resulting collision would lead the robot to stop (i.e., losing a momentum of $m_R \cdot v_R^n$). Depending on the application, other metrics can be developed. We present in the next section the development of a more complicated metric allowing the robot to navigate through unstructured obstacle like tall grass by lifting the approximation that all obstacles have infinite masses.

3.4 Taking into account the mass of the obstacles

In the context of autonomous navigation, the robot might have to go through obstacles for the point of view of the lidar, but are in fact harmless for the robot. An ideal example of this scenario is where the robot have to go through tall grass to reach its goal. Figure 7 shows the sensors measurements of a robot trying to go through tall grass. Since the lidar returns very close measurements around the robot, the robot would be unable to move. However, with the images provided by the camera, an algorithm could clearly detect that the obstacles are only tall grass, hence the robot should proceed and reach its goal.

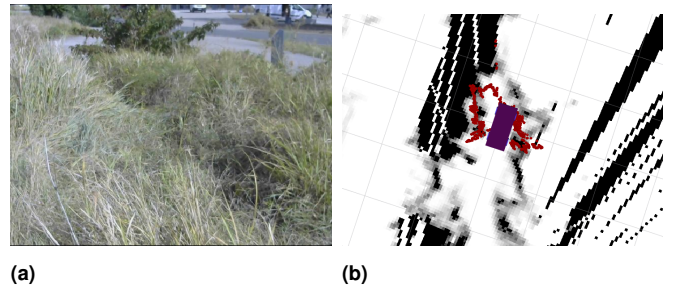


Figure 7. The robot crosses an area with tall grass. (a) Camera view of the robot. (b) Lambda-Field created from lidar measurements in red, with the robot in purple. The darker the cell, the higher the lambda is. Without mass estimation, the robot would not move as it is certain that a collision will happen.

As the risk metric developed in the previous section assumes that every obstacle has an infinite mass, it is unable to deal with such scenarios. This assumption is then removed and each obstacle has now a probabilistic mass. We thereby need to estimate the mass of the obstacles. It can be done with a camera and deep learning segmentation like Badrinarayanan et al. (2017) or radar classification as done by Lalonde et al. (2006). We also take into account that the mass of an obstacle is probabilistic. In addition to the Lambda-Field, we also store a map of the probability distribution function of the mass distribution for each cell, which is provided by one of the above cited methods.

Figure 8 shows examples of probability distribution function for several obstacles. The main use of a probabilistic formulation for the masses is to deal with the uncertainty of the labels. Indeed, the grass can easily hide a high density obstacle like rocks. Moreover, the mass of the vegetation is very variable and the robot can expect a harmless collision as much as a harmful collision, while going through this kind of obstacles. In the case where no label is available for a cell, the worst case is taken into account, meaning that the mass of the cell is set to infinity.

We chose to discretize the probability density function into a sum of Dirac impulses $\delta(\cdot)$. The mass p.d.f $f_i^m(\cdot)$ of the cell c_i is then

$$f_i^m(m) = \sum_{k=0}^{\infty} \alpha_{ik} \cdot \delta(m - k\Delta_m), \quad (23)$$

with Δ_m the discretization step and α_{ik} the probability that $m \in [k\Delta_m, (k+1)\Delta_m]$. Also, only a finite number of α_{ik} are not null in order to store the p.d.f.

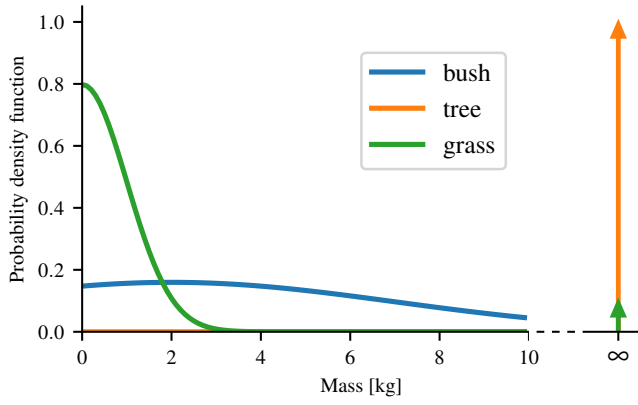


Figure 8. Examples of probability density function (p.d.f) of several labels. The arrow represents the Dirac delta function. The mass of the grass is very likely to be close to zero but there is a chance that a high-mass obstacle is hiding in it (e.g., a rock). The mass of a bush is very uncertain as it may be more or less dense. In the other way, the mass of a tree is always very high.

A problem quickly arises from Equation 20 if we want to take into account the mass of the obstacles. The equation only looks at the first collision as it assumes that any collision would lead the robot to stop its course. For very light obstacles like grass this assumption falls apart. Hence, we need to add a term to the equation to allow the robot to continue its course after a collision. To do so, we need to understand the meaning of the lambdas. For an area Δa where the lambda-field is constant with a value λ , the expected number of event ‘collision’ is λ . Using the probability $p_t(s)$, the probability of the robot being stopped because of the collision at the position s , we want that each collision has the probability p_t to be harmful for the robot. Hence, we use our probability of traversal $p_t(s)$ as a new measure over the field. The intensity function $\Lambda(\mathcal{C})$ is pondered by the harmful probability p_{ti} for the cell c_i , becoming

$$\Lambda_m(\mathcal{C}) = \Delta a \sum_{c_i \in \mathcal{C}} \lambda_i p_{ti} \quad (24)$$

Assuming that the robot can go through obstacles if their mass is below a certain threshold m_{\max} , the probability p_{ti} is then

$$\begin{aligned} p_{ti} &= \mathbb{P}(m_i < m_{\max}) \\ &= \int_0^{m_{\max}} f_i^m(m) dm, \end{aligned} \quad (25)$$

where $f_i^m(\cdot)$ is the p.d.f of the mass of the cell c_i . Also, since we do not assume anymore that the obstacles have infinite masses, the risk $r(\cdot)$ (i.e., the loss of momentum at the impact) becomes

$$\begin{aligned} r_m(\Delta ai, m) &= m_R \left(v_R^n(\Delta ai) - \frac{m_R v_R^n(\Delta ai)}{m_R + m} \right) \\ &= m_R \frac{m \cdot v_R^n(\Delta ai)}{m_R + m}, \end{aligned} \quad (26)$$

where m is the mass of the i th cell. Since the mass of each obstacle is probabilistic, we need to sum over all the possible masses to find the expected force of collision over a path,

leading to (the proof is detailed in Appendix B):

$$\begin{aligned} \mathbb{E}[r_m(A, M)] &= \sum_{i=0}^{N-1} K_i \int_0^{\infty} f_i^m(m) r(\Delta ai, m) dm \\ &= \sum_{i=0}^{N-1} K_i \sum_{k=0}^{\infty} \alpha_{ik} r(\Delta ai, k \Delta_m). \end{aligned} \quad (27)$$

where M is the random variable corresponding to the mass of the cell the collision happened, and K_i is computed the same way as in Equation 20 but using $\Lambda_m(\cdot)$. One can note that we can re-write the above equation under the form

$$\begin{aligned} \mathbb{E}[r_m(A, M)] &= \sum_{i=0}^{N-1} K_i r'(\Delta ai) \\ \text{with } r'(\Delta ai) &= \sum_{k=0}^{\infty} \alpha_{ik} r_m(\Delta ai, k \Delta_m), \end{aligned} \quad (28)$$

hence going back to the known expectancy formula of Equation 20. We omitted the parameters α_{ik} in the parameters of $r'(\cdot)$ as they are directly retrievable from the crossed area Δai . Also, one can note that setting $\mathbb{P}(m_i = \infty) = 1$ for all the cells leads as expected to the same risk as using Equation 21.

Using this metric, a robot can choose to take a path which leads to collisions, but is harmless for it. However, it will be the same for the robot to take a path without any collision of a path with harmless collisions that do not stop the robot. For manned vehicles, a path with collisions will always be more uncomfortable for the user. Hence, we define a metric called the *mean risk* over a path. This quantity is fitted to choose between safe paths, as the mean risk cannot assure the safety of a path. Indeed, for a path with a lot of harmless collisions and a harmful collision, the mean risk will be very close to the harmless collisions because of the quantity disparity. The mean risk is defined as the mean collision the robot will undergo, computed as

$$\bar{r} = \sum_{i=0}^{N-1} \frac{\Delta a \lambda_i r(\Delta ai)}{\sum_{j=0}^N \Delta a \lambda_j}. \quad (29)$$

As the lambdas can be very large, a more convenient form can be found:

$$\bar{r} = \sum_{i=0}^{N-1} \frac{r(\Delta ai)}{\sum_{j=0}^N \lambda_j \lambda_i^{-1}} \quad (30)$$

where $\lim_{(\lambda_i, \lambda_j) \rightarrow (\infty, \infty)} \lambda_j \lambda_i^{-1} = 1$.

3.5 Comparison and improvement of the reachability metric

In this section, we analyze and adapt the concept of *reachability* defined in Heiden et al. (2017). Their work is indeed the first to address the problem of risk assessment in occupancy grid shown in Figure 1. We first investigate the different metrics proposed in the article and then show that our framework can be seen as a generalization of their method. They propose to use the concept of product integrals, which is the product counterpart of the standard

integration. A summary of the product integration can be found in (Slavík 2007). At first, they define the reachability R_t for a path from the time $t = 0$ to T as

$$R_t = \prod_0^T (1 - m(x(t)))^{dt}, \quad (31)$$

where $x(t)$ is the robot position at the time t and $m(x(t))$ the probability that the position $x(t)$ is occupied. The higher the reachability is, the safer is the corresponding path. However, they say that it would be better to consider the distance travelled through a cell instead of the time. It is indeed better as the first metric leads to a counter-intuitive reachability: for a robot crossing at a speed v a straight path of length l , where all cells have the probability m of being occupied, the reachability is

$$\begin{aligned} R_t &= \prod_0^{l/v} (1 - m)^{dt} \\ &= \lim_{\Delta t \rightarrow 0} \prod_{i=0}^{l/v/\Delta t} (1 - m)^{\Delta t}. \end{aligned} \quad (32)$$

Using the fact that $(1 - m)^{\Delta t} = \exp(\ln(1 - m)\Delta t)$ and the Riemann definition of the integral, the expression can be simplified to

$$\begin{aligned} R_t &= \exp\left(\int_0^{l/v} \ln(1 - m) dt\right) \\ &= (1 - m)^{l/v}. \end{aligned} \quad (33)$$

The reachability from the first metric is then higher when the speed is high, meaning that it is safer to travel the path at higher speed.

Their second reachability metric R_L does not possess such behavior as they parametrized the integral over the distance travelled $L(t, t + dt)$ between two instants, leading to

$$\begin{aligned} R_L &= \prod_0^T (1 - m(x(t)))^{L(t, t+dt)} \\ &= \prod_0^T (1 - m(x(t)))^{|\dot{x}(t)| dt}. \end{aligned} \quad (34)$$

Since the travelled distance $d(t)$ equals to $\int_0^t |\dot{x}(t)| dt$, we have $dd(t) = |\dot{x}(t)| dt$ and the above expression can be simplified to

$$\begin{aligned} R_L &= \prod_0^D (1 - m(x_d(d)))^{dd} \\ &= (1 - m)^D \quad \text{in case of homogeneous field,} \end{aligned} \quad (35)$$

where $D = \int_0^T |\dot{x}(t)| dt$ is the distance travelled by the robot and $x_d(\cdot)$ the position of the robot as a function of the travelled distance. Using this equation, the probability of collision does not depend on the tessellation size nor the speed of the vehicle. The main drawback is that there is no natural reason to use the concept of product integrals, as it is here merely a tool to make the probability constant.

Furthermore, the robot is considered to be reduced to a point. The well-known solution to this problem is to inflate the obstacles, but it means that the robot is round.

We extend their theory to take into account the robot's width W . Instead of only integrate over the robot line path, we also, for each position $x_d(d)$, integrate over the entire width of the robot. The equation becomes

$$R_L = \prod_0^D \prod_{-W/2}^{W/2} (1 - m(x(d, w)))^{dw dd}, \quad (36)$$

where $x(d, w)$ is a point of the robot parametrized as the distance the robot has travelled d and the distance from robot header center in its width direction w .

We can see that for the special case $W = 1$ and $m(x(d, w))$ constant for $w \in [-W/2, W/2]$ we go back to their equation. We can from here develop a more convenient formulation for calculations. If the robot crosses the N cells $\mathcal{C} = \{c_i\}$ of size $S \times S \text{ m}^2$ and of probability of occupancy m_i , the above equation can be re-arranged to give

$$\begin{aligned} R_L &= \prod_{i=0}^{N-1} \prod_{x=0}^S \prod_{y=0}^S (1 - m_i)^{dx dy} \\ &= \prod_{i=0}^{N-1} (1 - m_i)^{\Delta a}, \end{aligned} \quad (37)$$

where $\Delta a = S^2$ is the area of each cell.

One interesting thing is that this equation can be linked to the theory of Lambda-Field. Indeed, for a path crossing the cells $\mathcal{C} = \{c_i\}$, we have in the Lambda-Field

$$\begin{aligned} 1 - \mathbb{P}(\text{coll}) &= \exp\left(-\Delta a \sum_{c_i \in \mathcal{C}} \lambda_i\right) \\ &= \prod_{c_i \in \mathcal{C}} \exp(-\lambda_i)^{\Delta a} \\ &= \prod_{c_i \in \mathcal{C}} (1 - m_i)^{\Delta a} \quad \text{with } m_i = 1 - \exp(-\lambda_i). \end{aligned} \quad (38)$$

Hence, we see that the probability of occupancy m_i of a cell is the probability of colliding in an area of 1 m^2 in a Lambda-Field. Under our improvement, the theory of Heiden et al. (2017) is then a special case of our framework, where the risk function $r(\cdot)$ is set to 1.

4 EXPERIMENTATIONS

4.1 Setup

In order to test our theory, we implemented our framework into a robot equipped with a lidar LMS151 and a camera as shown in Figure 10. Since the robot has four-wheel steering, it was not much impacted by slipping and skidding and the odometry was sufficient to estimate the robot displacements. For every new lidar scan, the displacement between the current and previous position is estimated and the map is updated. Furthermore, the map is centered on the robot. We chose not to rotate the map but to rotate the robot instead to nullify the errors coming from the rotation. Indeed, a straight wall is quickly distorted after a few rotations because of

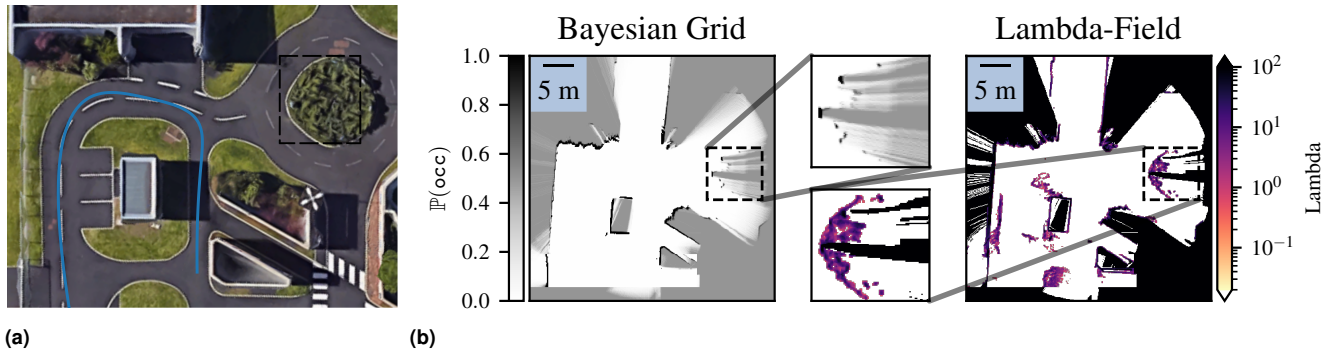


Figure 9. (a) Aerial View of the mapped environment, with the robot path in blue and the roundabout in dashed black (b) *Left:* Bayesian occupancy grid *Right:* Lambda-Field. The Lambda-Field is better suited to store the occupancy of unstructured obstacles where the Bayesian Occupancy Filter may over-converges, especially for the roundabout (dashed black).

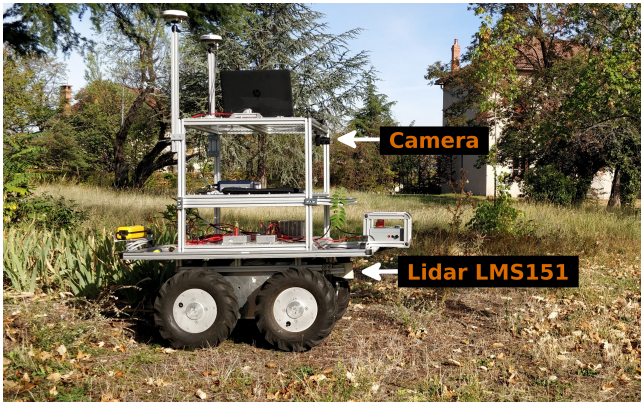


Figure 10. The robot used in the experimentations. It is equipped with a lidar Sick LMS151 and a camera.

the tessellation of the map. We also had to keep a global offset of the map as otherwise small displacements were not taken into account. Indeed, without this offset the map is not precisely updated as any displacement below half the cell size is discarded. The mass of the robot is also set to $m_R = 50$ kg. For safety purpose, the maximum speed of the robot was set to 0.5 m s^{-1} and the maximum acceleration to 0.05 m s^{-2} .

The normals of the obstacles were estimated using the method developed in [Senanayake and Ramos \(2018\)](#). At each lidar scan the normal of each point is estimated and the normals of the underlying cells are updated as follows:

$$\bar{\theta} = \begin{cases} \arctan(\bar{S}/\bar{C}) & \text{if } \bar{C} \geq 0 \\ \arctan(\bar{S}/\bar{C}) + \pi & \text{otherwise,} \end{cases} \quad (39)$$

with

$$\bar{C} = \sum_{i=1}^N \cos(\theta_i) \quad \text{and} \quad \bar{S} = \sum_{i=1}^N \sin(\theta_i), \quad (40)$$

where N is the number of normal measurements θ_i for the cell c_i .

4.2 Mapping

We first demonstrate the effectiveness of the mapping using Lambda-Field. To do so, we implemented a simple robot follower scenario in an urban-like environment. The robot

had to follow the pedestrian while keeping the risk of the chosen path below 5 kg m s^{-1} . While following the pedestrian, the robot created a Lambda-Field as well as a Bayesian occupancy grid of the environment, as shown is [Figure 9](#). The parameters used for the mapping were $p^m = 0.9999$ and $p^h = 0.99$ for all cells measurements. The value of p^m is intentionally very high as it is indeed nearly impossible for a lidar beam to go through obstacles. The environment did not contain obstacles like glass walls where the lidar beams could go through. If it was the case, the probability p^h should be lowered. The Lambda-Field was discretized into 501×501 cells of 0.1×0.1 m centered on the robot. [Figure 9](#) shows the Lambda-Field as well as the Bayesian occupancy grid while [Figure 11](#) shows the confidence intervals of the lambdas.

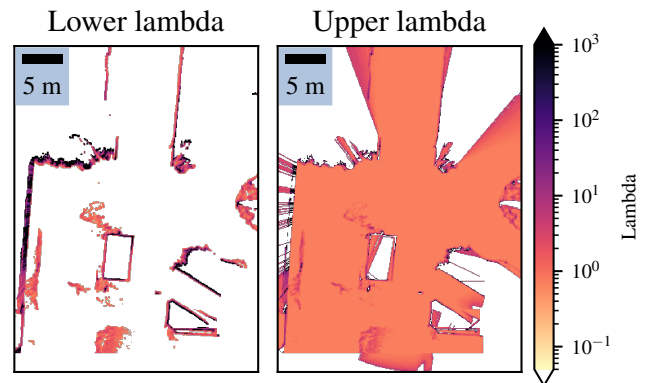


Figure 11. Difference of lambdas between the expected lambdas and the confidence interval for a structured environment. The lower lambdas tend to underestimate the obstacles as the expected lambdas in the free space are already at the lowest value. The upper lambdas overestimate the field everywhere, particularly where few measurements were available, like in the roundabout or behind the fence on the left.

The comparison is not easy as the Lambda-Field does not store the same information as the Bayesian occupancy grid. However, the maps are globally alike except for the unstructured obstacles, which are in this case the bushes in the roundabout as well as tall grass around the pavement. As the Bayesian occupancy grid needs to converge to either the state ‘occupied’ or ‘free’, a lot of information about the occupancy of the roundabout is discarded. Using Lambda-Field, most of the information is preserved and the

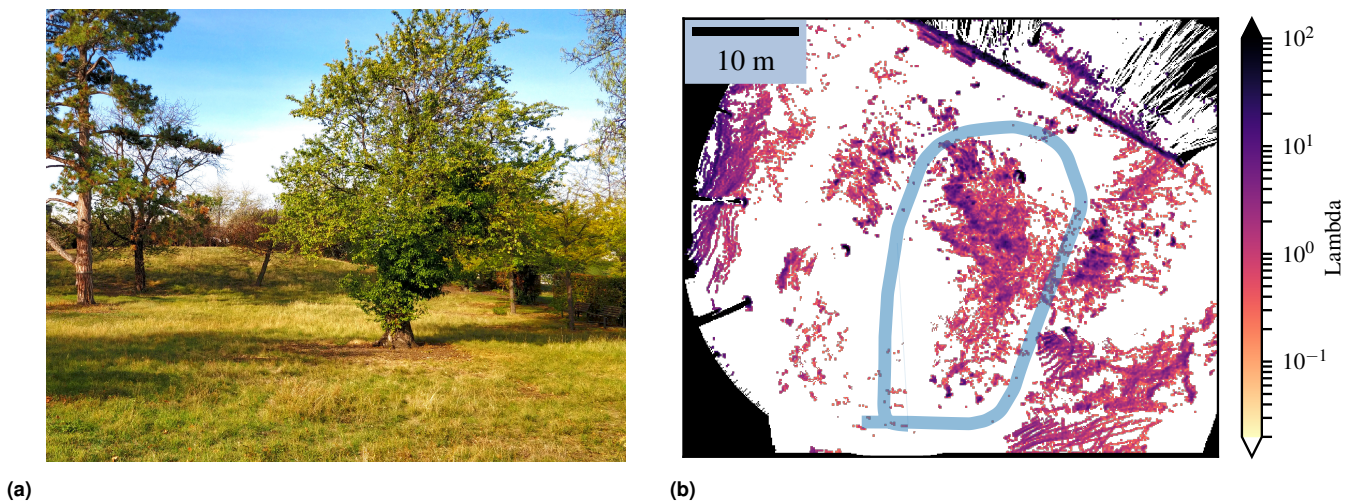


Figure 12. Mapping of an unstructured zone. (a) The robot, with its path in light blue, went around the nearest tree on the picture, before going back to its initial position. (b) Because of the tall grass, the map stored a lot of obstacles during the traversal. The tree trunk is still visible as they have much higher lambdas.

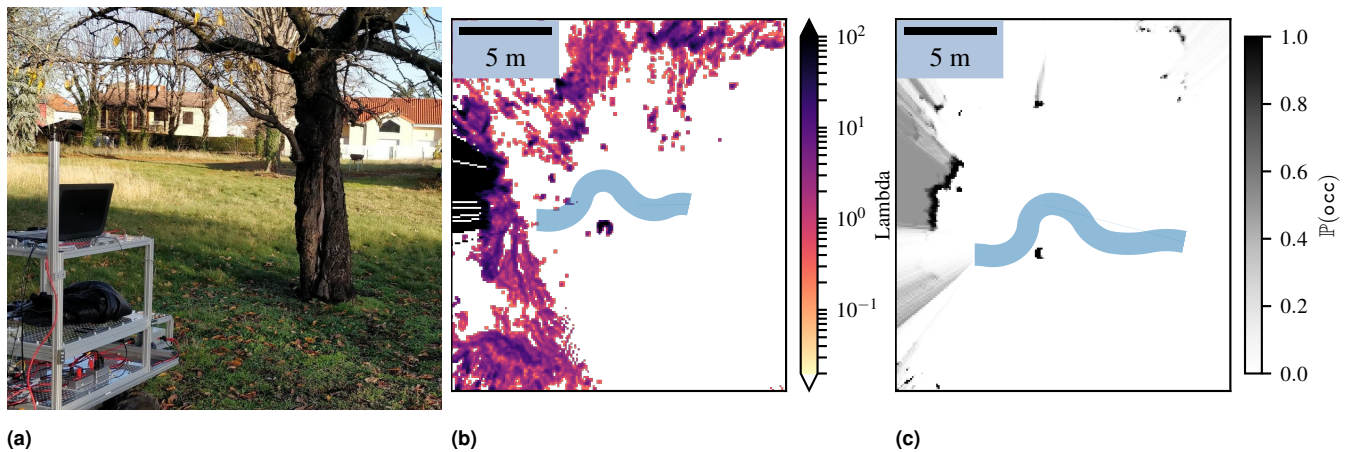


Figure 13. The robot has to avoid a tree which was on its path. (b) Lambda-Field with the path the robot has taken in light-blue. (c) Bayesian occupancy grid with the path the robot has taken in light-blue.

global shape of the roundabout is more easily seen. The other disparities between the two maps also come from unstructured obstacles which were small trees and tall grass.

In addition to the expected lambdas, the Lambda-Field also stores a confidence interval for each value. Figure 11 shows the difference between the expected lambdas λ_i and the lower and upper values λ_L, λ_U of the confidence interval. It can be easily seen that the lower lambdas only underestimate the lambdas for the obstacles. Indeed, the expected lambda is already at the lowest possible value, zero, for the cells where no collision has happened. They can however be useful in case where a lot of faulty measurements come from the sensor, for example when lidars try to map an environment under heavy rain or during a snowstorm. On the contrary, upper lambdas over estimate the lambdas for regions where few measurements are available. It is specially the case in the roundabout or in the boundary of the map, as well as behind the fence on the left side of the map where only a few lidar beams went through.

In order to demonstrate the usability of our framework, we also mapped an unstructured environment shown in Figure 12. The environment consists of several trees with

a lot of tall grass tall disrupting lidar measurements. The robot went around the tree in the center of the picture while navigating in the grass. However, due to the grass and the wind, the lidar returned a lot of false measurements corresponding to the grass. As shown in Figure 12b, any standard path-planning algorithms would not work in this kind of environment, as there are obstacles almost everywhere. Even if the map is very noisy, the hedge is still clearly visible. The tree trunks are also perceptible from the tall grass by having a much higher lambda value.

4.3 Basic path planning

We demonstrate in this part that our framework can be used to do classical path planning. As shown in Figure 13a, the robot has to go around a tree to reach the goal which was set behind. To do so, we implemented the path planning algorithm of Gerkey and Konolige (2008). Every 3 seconds, we sample feasible commands for the robot and choose the best one. The best command (i.e., path) is the one that stay below a risk threshold and lead the robot the closest possible to the target, that was in this case behind the tree. The chosen path also had to have an upper risk (i.e., the risk computed

using the upper bound of the lambdas) below a certain risk threshold. For each feasible command, the N cells crossing the path induced by the command applied for 8 seconds are extracted and the risks are computed. Estimated the risk of a longer time than the one applied by the command avoids the robot to choose paths leading to a dead end. Indeed, if the risk was computed only for the time of the command, the applied command might lead the robot to be right in front of a wall in a configuration it is impossible to escape. In the case where no command meets the criteria, the robot stops. It can happen when the robot is at high speed: because of the limited deceleration, all the high speed commands lead to a risk which is too high. Then, the robot completely stops and continue its course as it can now sample low speed commands.

We also implemented the Reachability metric of Heiden et al. (2017) with our improvement to handle the robot size. As converting the Lambda-Field into an occupancy grid using Equation 38 would lead to computing the risk $r(\cdot) = 1$, hence using our theory, we used the bayesian occupancy grid directly computed from lidar measurements. Using the same method for path planning, we sample paths and choose the one which leads the closer to the goal, where a path is considered safe if its reachability R_L is above a certain threshold $1 - \epsilon, \epsilon \in]0, 1[$. The threshold ϵ was set to 0.1 during our experiments. For each applied command, 300 samples are evaluated.

Using both algorithms on a same environment allows the comparison of the behaviors of the robot in a simple case. Figure 13 shows the result of the path planning for the two environment representations. For the Lambda-Field, the maximum allowed expected risk was set to 0 kg m s^{-1} meaning that the robot must remain clear of any collision. We see that the paths are much alike and the robot effectively avoids the obstacles in both cases. It can be seen on the Lambda-Field that the robot path crossed some cells where the lambda is not null, which would lead to a collision. However, as the Lambda-Field is computed in real-time, the lidar measured collisions in this cell after the robot crossed it. The lidar beams can indeed go through the grass or returns a collision depending on the position of the robot.

The same experiment was conducted using different parameters for the Lambda-Field. Figure 14 shows the resulting speed of the robot for different configurations of parameters. While the robot had to expect no risk on its path, it was first allowed to have an upper risk at 5 kg m s^{-1} , meaning that we are sure at 95% that any unexpected collision has an expected risk below 5 kg m s^{-1} . The robot quickly reached its maximal speed with full acceleration while keeping the upper risk below the threshold. Under the same configuration, the robot had to reach the goal while keeping the upper risk below 2 kg m s^{-1} . As the upper risk is smaller, the robot had to reduce its speed. The robot has the same type of reaction if its confidence in the lidar sensor decreases. In the third experiment, the probability of right ‘miss’ measurement p^m was decreased from 0.9999 to 0.99. The direct implication is the confidence interval broadened, forcing again the robot to decrease its speed. Then, the robot had a poor confidence in the lidar as well as a small upper risk, leading to a very slow traversal speed. Thereupon, the Lambda-Field allows classical path planning in the same

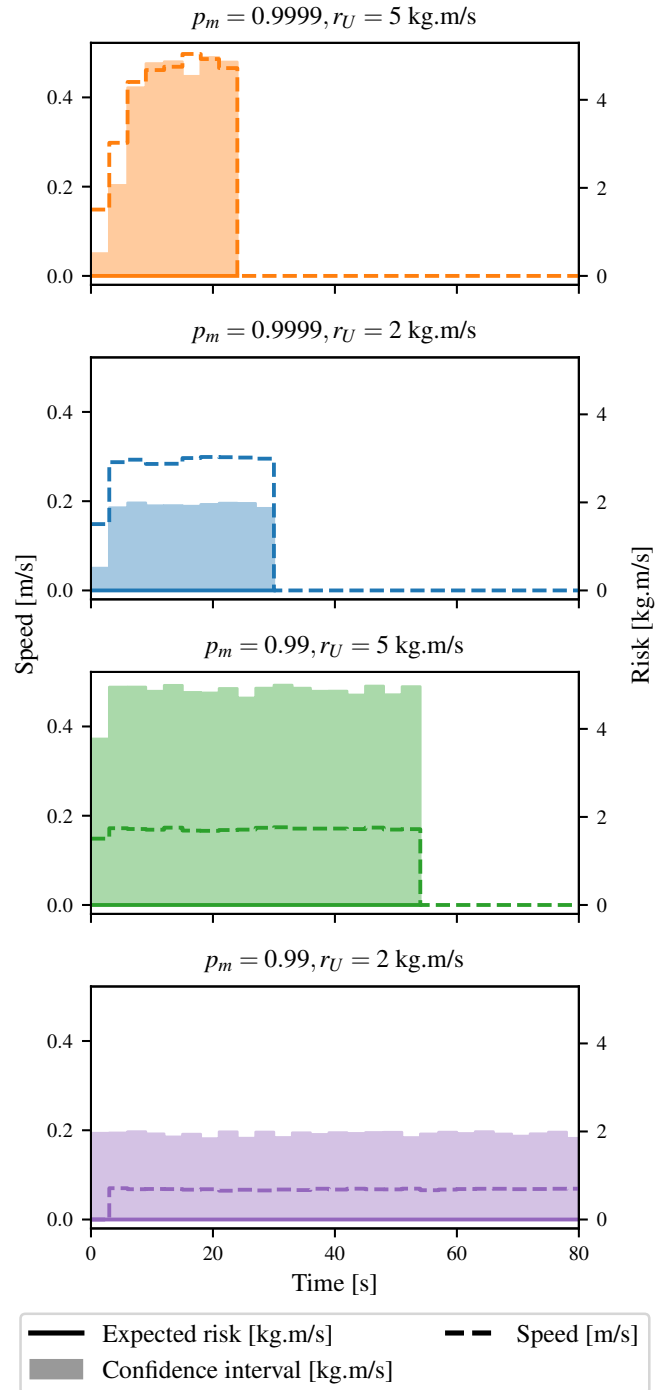


Figure 14. Speed (dashed line) and risk (solid line with dashed area for its confidence interval) of the chosen paths of the robot going around a tree for different configurations. The robot is able to navigate at a higher speed when it is confident about the measurements and has a higher upper risk limit.

fashion as Heiden et al. (2017). Our framework also regulates the speed of the robot to cope with the allowed risk level.

4.4 Going through tall grass

After doing simple path planning, we show that the Lambda-Fields allow the robot to navigate in unstructured environments. As shown in Figure 15a, the robot has to reach the goal which is behind tall grass. This kind of environment leads to very noisy maps which can hinder

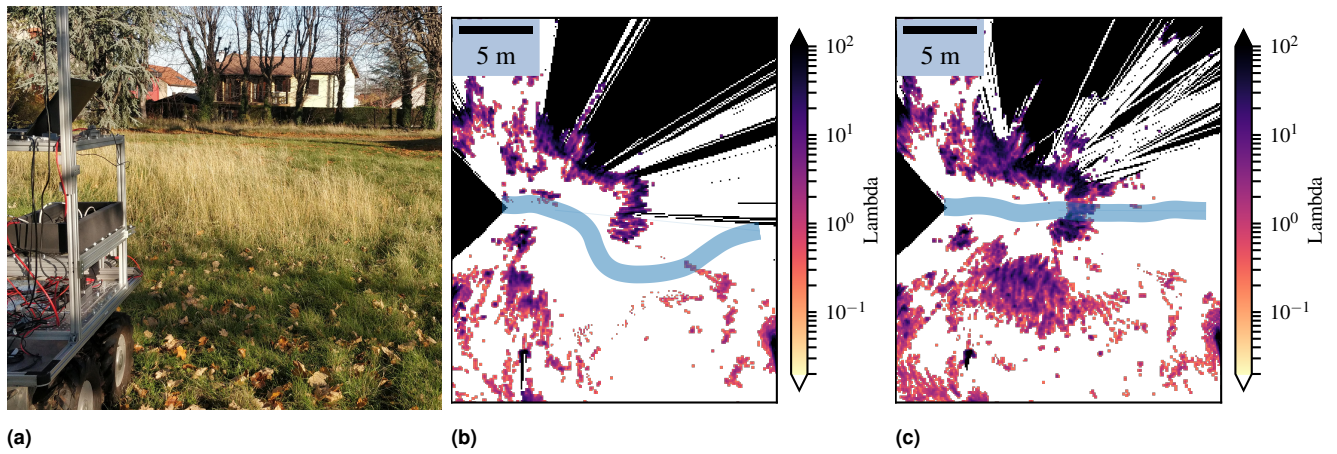


Figure 15. The robot has to reach a goal behind the tall grass. (b) Lambda-Field with the path the robot has taken in blue, where the robot was instructed to take absolutely no risk. (c) Lambda-Field with the path the robot has taken in blue, where the robot was allowed to take some risk.

robot's displacements if looking at the probability of collision.

We here show that according to the risk the robot is willing to take, it chooses to either go through the tall grass or trying to find a path around it. This kind of behavior is impossible to have when only looking at the probability of collision. Indeed, the robot is sure to collide the grass. The probability of collision is high but the collision engendered by the grass is harmless, leading to a very small risk.

First, the robot knows that the obstacles in front of it is tall grass using a camera. For any other zone, the mass is set to the worst case (i.e., $\mathbb{P}(m_i = \infty) = 1$) as any other prior may lead to under-estimate the risk. We assumed that tall grass has a 95% chance to have a null mass and a 5% chance of having an infinite mass. This probability models the possibility that tall grass can hide very dense obstacles like rocks or tree trunks.

Two cases are analyzed: in the first one, the robot had to take no risk, meaning that for every path the robot takes, the expectation of the risk has to be zero. Hence, the robot chose to go around the tall grass. In the second case, the robot was allowed to take some risk to reach its goal and went through the tall grass. **Figure 15** shows the resulting Lambda Fields for these two different robot configurations. In the first case, since the tall grass has a non-zero probability to have a mass which leads to a harmful collision, the robot chooses to go around the tall grass to reach the goal. Once again, the cells with a lambda higher than zero on the path of the robot have been updated after the robot went through it. At the time the robot crossed these cells the lambdas were null. **Figure 16** shows the speed as well as the risk taken by the robot. The robot first crosses a zone where the mass is supposed to be low, leading to a very narrow confidence interval. The confidence interval grows quickly as the robot goes out of the low mass zone. The robot also stopped several times during the traversal. Indeed, a lot of grass hindered its movements as the detection of the grass is very random. Because of the maximum deceleration of the robot, no path were below the maximum risk allowed. The robot then had no choice but to completely stop to be able to plan with low speed commands.

In the second case, the robot was allowed to take some risk and chose to go through the tall grass to reach the goal.

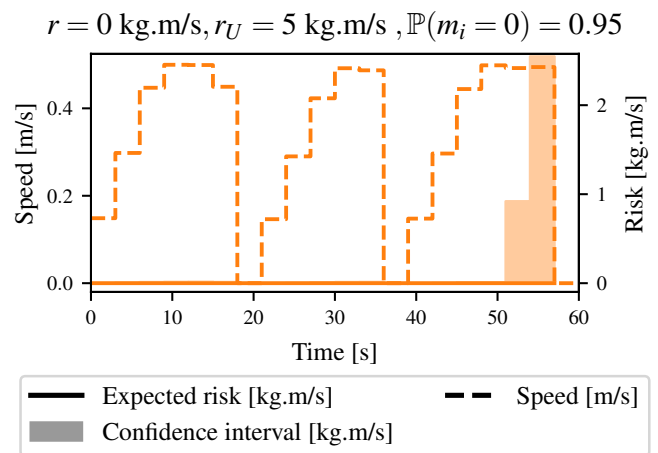


Figure 16. Speed (dashed line) and risk (solid line with dashed area for its confidence interval) of the chosen paths of the robot when it chooses to go around the tall grass. The numerous stops of the robot are due to the very random detection of the tall grass.

The differences of lambdas between the two maps come from the fact that depending on the robot position, the lidar beams can go through the grass or return a collision. Furthermore, there was a lot of wind during the experimentations, leading to an accentuation of the noise of the overall map. For this case, different configuration of risk were analyzed. **Figure 17** shows the speed as well as the risk taken by the robot. In the first configuration, the robot entered the grass at $t \approx 12$ s. It was allowed to have an expected risk of 0.1 kg m s^{-1} and an upper risk of 5 kg m s^{-1} . The grass had 5% chance of having an infinite mass. The robot stopped at $t \approx 18$ s as it was about to enter a denser zone, meaning a zone with a higher collision probability. All the high speed commands lead to a too high risk and the robot had to completely stop. During the traversal of the tall grass, the speed of the robot was maintained to a low value as the grass might hide an obstacle. As the robot goes out of the grass at $t \approx 36$ s, it increases its speed to its maximum since a collision is more unlikely to happen. The same experiment was conducted where this time the grass zone had a probability of 99% to have a null mass. The robot stopped in the same place as the first time, but

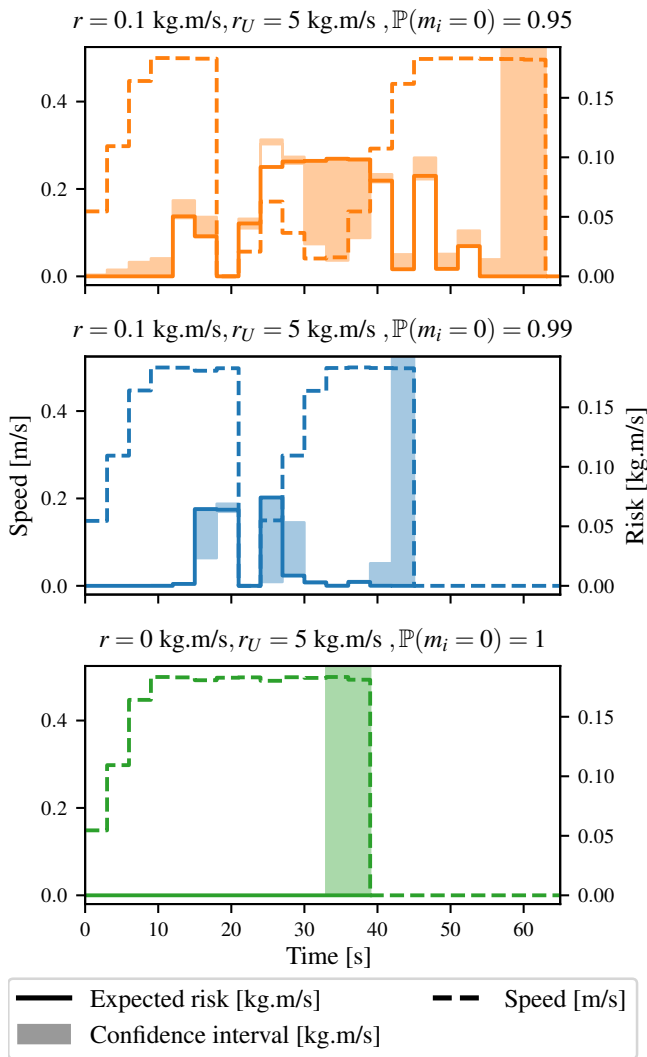


Figure 17. Speed (dashed line) and risk (solid line with dashed area for its confidence interval) of the chosen paths of the robot when it chooses to go through the tall grass, for different configurations. The more certain the robot is that there are no obstacles in the grass, the faster it reaches its goal.

increased faster its speed as it was surer than the collisions were harmless. By doing so, it reached quicker the goal. In the third time, the robot was sure there was no obstacle in the grass. Hence, it crossed at full speed the environment since any collision was harmless even if the maximum risk allowed was null.

A very specific event can appear as sometimes, the expected risk is outside the confidence interval. It can be seen for $t = 25$ s on the first graph of Figure 17. Computing the risk with lower lambdas can indeed lead to a higher risk in very specific conditions. In our case, the robot computed the risk for a path going out of the null mass zone. By doing so, any collision happening outside this zone will have a higher expected force of collision. It is then considered less risky to collide inside the null mass zone: lowering the lambdas leads to a higher chance to collide outside as the robot has a lower chance to be stopped inside the zone, leading to a higher risk.

5 Discussion

As said before, the theory of the lambda-Field can be seen as a generalization of the framework of Heiden et al. (2017). Under this consideration, it is possible to convert a Lambda-Field into a Bayesian occupancy grid and vice versa using Equation 38. In addition to adding meaning to the equations of Heiden et al. (2017), our framework allows the computation of expectancy of a risk. It is possible as the Lambda-Field possesses a probability density function.

The theory of Poisson Point Process has already been used by Eggert (2014) for known obstacles. The Lambda-Field can be seen as the transposition of their work for occupancy grids.

However, one of the major drawbacks of the Lambda-Field is the assumption done in Equation 7. Using such approximation indeed leads to inflate the obstacles, meaning that some narrow corridors where the robot could go through becomes impracticable. The modeling of the sensor can also be discussed: for practical reasons, the sensor is assumed to have a deterministic error region where the collision is sure to have happened. Taking a too small error region would lead to augment the probability of wrong measurements, increasing the confidence interval of the lambdas hence decreasing the speed of the robot. Inversely, taking a too big error region leads to inflate the obstacles hence decreasing the space the robot can evolve in.

Also, some issues can appear while estimating the risk with our framework for global path planning algorithms. Indeed, it may be harder to understand the metrics. The longest the path, the higher will be the risk. As this behavior seems intuitive, it leads to several questions. For two paths with the same risk but a different length, are we willing to take the two paths with the same confidence? Or should we ponder the risk by the length of the path, meaning that we are willing to take more risk for longer paths? We chose to understand the risk as the risk of a given command. Indeed, we believe that as humans, we assess the risk of every step we make without thinking about the length of the path.

Furthermore, the expectancy of the risk is not fitted to model the ‘long-tail’ of the gaussian, meaning the low-probability events that can happen. The faulty measurements of the lidar are coped with the confidence intervals of the lambdas but other metrics may better estimate the ‘long-tail’. The Conditional Value at Risk presented by Majumdar and Pavone (2020) explicitly measures the risk of the ‘long-tail’. It can then be a better indicator of the risk for situations where a low probability high risk situation is present, like for example when a high mass obstacle hides in the grass.

Future works will also add dynamic obstacles to deal with urban-like environments. Under such scenarios, the robot will also need to model occluded areas such as crossroads.

6 CONCLUSION

We presented in this article a novel representation of the occupancy information of the environment, called Lambda-Field. We first derived a way to construct the map, as well as confidence intervals over these values. This representation allows computation of expectancy over a path, giving a natural way to assess different types of risks. The Lambda-Field is very alike the Bayesian occupancy grid for mapping,

with the only notable difference that the Lambda-Field better store unstructured obstacles like bushes or tall grass. In addition, the Lambda-Field provides the computation of a generic risk that depends on the application.

In the case of unmanned ground vehicles, we chose to represent the risk as the force of collision. In contrast to risk metrics defined on Bayesian occupancy grid, our risk possesses a physical meaning. We were able to control the level of risk the robot could take over its planning, giving behaviors impossible with classical path planning environment representations. The robot was indeed allowed to cross low mass occupied areas such as tall grass as long as the risk level was low enough. Therefore, the Lambda-Field provides a framework that regulates the path as well as the speed of the robot, ensuring the robot's safety.

Funding

This work was sponsored by a public grant overseen by the French National Research Agency as part of the "Investissements d'Avenir" through the IMobS3 Laboratory of Excellence (ANR-10-LABX-0016), the IDEX-ISITE initiative CAP 20-25 (ANR-16-IDEX-0001) and the RobotEx Equipment of Excellence (ANR-10-EQPX-0044).

References

- Agha-mohammadi AA, Heiden E, Hausman K and Sukhatme G (2019) Confidence-rich grid mapping. *International Journal of Robotics Research* : 1–23.
- Badrinarayanan V, Kendall A and Cipolla R (2017) SegNet: A Deep Convolutional Encoder-Decoder Architecture for Image Segmentation. *IEEE Transactions on Pattern Analysis and Machine Intelligence* 39(12): 2481–2495.
- Caborni C, Ko SY, De Momi E, Ferrigno G and Y Baena FR (2012) Risk-based path planning for a steerable flexible probe for neurosurgical intervention. *Proceedings of the IEEE RAS and EMBS International Conference on Biomedical Robotics and Biomechatronics* (0): 866–871.
- Čikeš M, Dakulovič M and Petrovič I (2011) The path planning algorithms for a mobile robot based on the occupancy grid map of the environment - A comparative study. *2011 23rd International Symposium on Information, Communication and Automation Technologies, ICAT 2011* .
- Coué C, Pradalier C, Laugier C, Fraichard T and Bessière P (2006) Bayesian occupancy filtering for multitarget tracking: An automotive application. *International Journal of Robotics Research* 25(1): 19–30.
- De Filippis L, Guglieri G and Quagliotti F (2011) A minimum risk approach for path planning of UAVs. *Journal of Intelligent and Robotic Systems: Theory and Applications* 61(1-4): 203–219.
- Dhawale A, Yang X and Michael N (2018) Reactive Collision Avoidance Using Real-Time Local Gaussian Mixture Model Maps. *IEEE International Conference on Intelligent Robots and Systems* : 3545–3550.
- Eggert J (2014) Predictive risk estimation for intelligent ADAS functions. *2014 17th IEEE International Conference on Intelligent Transportation Systems, ITSC 2014* : 711–718.
- Elfes A (1989) Using occupancy grids for mobile robot perception and navigation. *Computer* 6: 46–57.
- Feyzabadi S and Carpin S (2014) Risk-aware path planning using hierarchical constrained Markov Decision Processes. *IEEE International Conference on Automation Science and Engineering* : 297–303 DOI:10.1109/CoASE.2014.6899341.
- Fraichard T (2007) A Short Paper About Motion Safety. *IEEE International Conference on Robotics and Automation* : 1140—1145.
- Francis G, Ott L and Ramos F (2018) Functional Path Optimisation for Exploration in Continuous Occupancy Maps. *Workshop on Informative Path Planning and Adaptive Sampling (ICRA 2018)* .
- Fulgenci C, Spalanzani A and Laugier C (2007) Dynamic obstacle avoidance in uncertain environment combining PVOs and occupancy grid. *IEEE International Conference on Robotics and Automation* : 1610–1616.
- Fulgenci C, Spalanzani A and Laugier C (2009) Probabilistic motion planning among moving obstacles following typical motion patterns. *2009 IEEE/RSJ International Conference on Intelligent Robots and Systems, IROS 2009* : 4027–4033.
- Fulgenci C, Tay C, Spalanzani A and Laugier C (2008) Probabilistic navigation in dynamic environment using Rapidly-exploring Random Trees and Gaussian Processes. *IEEE/RSJ International Conference on Intelligent Robots and Systems* : 1056—1062.
- Gerkey B and Konolige K (2008) Planning and control in unstructured terrain. *ICRA Workshop on Path Planning on Costmaps* .
- Guizilini V, Senanayake R and Ramos F (2019) Dynamic hilbert maps: Real-time occupancy predictions in changing environments. *Proceedings - IEEE International Conference on Robotics and Automation 2019-May*: 4091–4097.
- Heiden E, Hausman K and Sukhatme GS (2017) Planning High-speed Safe Trajectories in Confidence-rich Maps. *IEEE/RSJ International Conference on Intelligent Robots and Systems* : 2880—2886.
- Joachim S, Tobias G, Daniel J and Riidiger D (2008) Path planning for cognitive vehicles using risk maps. *IEEE Intelligent Vehicles Symposium, Proceedings* : 1119–1124.
- Kim S and Kim J (2013) Continuous occupancy maps using overlapping local Gaussian processes. *IEEE International Conference on Intelligent Robots and Systems* : 4709–4714.
- Kraetzschmar GK, Gassull GP and Uhl K (2004) Probabilistic quadrees for variable-resolution mapping of large environments. *Proceedings of the 5th IFAC/EURON symposium on intelligent autonomous vehicles* .
- Laconte J, Debain C, Chapuis R, Pomerleau F and Aufrère R (2019) Lambda-Field : A Continuous Counterpart of the Bayesian Occupancy Grid for Risk Assessment. *IEEE/RSJ International Conference on Intelligent Robots and Systems (IROS)* : 167–172.
- Lalonde JF, Vandapel N, Huber DF and Hebert M (2006) Natural terrain classification using three-dimensional lidar data for ground robot mobility. *Journal of Field Robotics* 23(10): 839—861.
- Laugier C, Paromtchik IE, Perrollaz M, Yong M, Yoder JD, Tay C, Mekhnacha K and Nègre A (2011) Probabilistic analysis of dynamic scenes and collision risks assessment to improve driving safety. *IEEE Intelligent Transportation Systems Magazine* 3: 4–19.

- Lee DN (1976) A theory of visual control of braking based on information about time-to-collision. *Perception* 5: 437–459.
- Majumdar A and Pavone M (2020) How Should a Robot Assess Risk? Towards an Axiomatic Theory of Risk in Robotics. *Robotics Research* : 75—84.
- O’Callaghan ST and Ramos FT (2012) Gaussian process occupancy maps. *International Journal of Robotics Research* 31(1): 42–62.
- Pereira AA, Binney J, Jones BH, Ragan M and Sukhatme GS (2011) Toward risk aware mission planning for autonomous underwater vehicles. *IEEE International Conference on Intelligent Robots and Systems* : 3147–3153.
- Primatesta S, Guglieri G and Rizzo A (2019) A Risk-Aware Path Planning Strategy for UAVs in Urban Environments. *Journal of Intelligent and Robotic Systems: Theory and Applications* 95(2): 629–643.
- Ramos F and Ott L (2016) Hilbert maps: Scalable continuous occupancy mapping with stochastic gradient descent. *International Journal of Robotics Research* 35(14): 1717–1730.
- Rohou S, Jaulin L, Mihaylova L, Bars FL, Veres S, Rohou S, Jaulin L, Mihaylova L, Bars FL, Reliable SV, Rohou S, Jaulin L, Mihaylova L and Le F (2018) Reliable non-linear state estimation involving time uncertainties. *Automatica* 93: 379–388.
- Rummelhard L, Nègre A, Perrollaz M and Laugier C (2014) Probabilistic Grid-based Collision Risk Prediction for Driving Application. *Experimental Robotics* : 821–834.
- Saval-Calvo M, Medina-Valdés L, Castillo-Secilla JM, Cuenca-Asensi S, Martínez-Álvarez A and Villagrà J (2017) A review of the bayesian occupancy filter. *Sensors* 17: 344.
- Senanayake R and Ramos F (2017) Bayesian Hilbert Maps for Continuous Occupancy Mapping in Dynamic Environments. *Conference on Robot Learning* : 458–471.
- Senanayake R and Ramos F (2018) Directional grid maps: modeling multimodal angular uncertainty in dynamic environments. *2018 IEEE/RSJ International Conference on Intelligent Robots and Systems (IROS)* : 3241—3248.
- Slavič A (2007) *Product integration, its history and applications*, volume 1. Matfyzpress Prague.
- Tsardoulis EG, Iliakopoulou A, Kargakos A and Petrou L (2016) A Review of Global Path Planning Methods for Occupancy Grid Maps Regardless of Obstacle Density. *Journal of Intelligent and Robotic Systems* 84: 829–858.
- Tsiotras P and Bakolas E (2007) A hierarchical on-line path planning scheme using wavelets. *2007 European Control Conference, ECC 2007* : 2806–2812.
- Vaillant M, Davatzikos C, Taylor RH and Bryan RN (1997) A Path-Planning Algorithm for Image-Guided Neurosurgery. *CVRMed-MRCAS’97* : 467—476.
- Yang K, Keat Gan S and Sukkarieh S (2013) A Gaussian process-based RRT planner for the exploration of an unknown and cluttered environment with a UAV. *Advanced Robotics* 27(6): 431–443.

A Heterogeneous error regions

In the case that the error regions \mathcal{E}_k have a different size for each lidar beam b_k , we need to further approximate the derivative of the log-likelihood. Under the same assumption that the h_i error regions \mathcal{E}_k containing the cell c_i are small, we have

$$\begin{aligned} \frac{\partial \mathcal{L}(X|\lambda)}{\partial \lambda_i} &= -m_c \cdot \mathcal{A} + \sum_{k=0}^{h_i-1} \frac{\mathcal{A}}{\exp(e_k \lambda_i) - 1} \\ &\approx -m_c \cdot \mathcal{A} + \sum_{k=0}^{h_i-1} \frac{\mathcal{A}}{e_k \lambda_i}, \end{aligned} \quad (41)$$

leading to

$$\lambda_i = \frac{1}{m_i} \sum_{k=0}^{h_i-1} \frac{1}{e_k}. \quad (42)$$

This approximation over-estimates the lambdas compared to Equation 9. Indeed, in the special case where all the \mathcal{E}_k have the same area e , the computed lambdas from Equation 42 are

$$\lambda_i = \frac{1}{e} \frac{h_i}{m_i}. \quad (43)$$

As $\forall x \in \mathbb{R}_{\geq 0}, x \geq \ln(1+x)$, we will always over-estimate the lambdas using Equation 42. This is the desired behavior as under-estimating the lambdas would lead to under-estimate the risk.

B Proof of Equation 27

We here prove Equation 27. We have two random variables: the area at which the robot collides A and the mass M of the cell where the collision happened, of marginal probability density functions $f(\cdot)$ and $f^m(\cdot)$. Note that we do not have directly access to $f^m(\cdot)$ but only $f_i^m(\cdot) = f^m(\cdot | \Delta ai)$, the probability density function of the mass given where the collision happened. Under the assumption that the risk $r(\cdot)$ is constant inside each cell, the expectation of the function $r(A, M)$ is

$$\begin{aligned} \mathbb{E}[r(A, M)] &= \int_0^{N\Delta a} \int_0^\infty r_m(a, m) f(a) f^m(m|a) dm da \\ &= \sum_{i=0}^{N-1} \int_{i\Delta a}^{(i+1)\Delta a} f(a) \int_0^\infty r_m(a, m) f_i^m(m) dm da \\ &= \sum_{i=0}^{N-1} \left[\int_{i\Delta a}^{(i+1)\Delta a} f(a) da \right] \left[\int_0^\infty r_m(\Delta ai, m) f_i^m(m) dm \right] \\ &= \sum_{i=0}^{N-1} K_i \int_0^\infty r_m(\Delta ai, m_i) f_i^m(m_i) dm \\ &= \sum_{i=0}^{N-1} K_i \sum_{k=0}^\infty \alpha_{ik} r_m(\Delta ai, k\Delta m), \end{aligned} \quad (44)$$

for a path \mathcal{P} going through the cells $\{c_i\}_{0:N-1}$, and with $K_i = \exp(-\Lambda_m(\{c_j\}_{0:i-1})) [1 - \exp(-\Lambda_m(\{c_i\}))]$.